Journal of
Materials Chemistry A

ROYAL SOCIETY
OF CHEMISTRY

PAPER

View Article Online
View Journal | View Issue

Cite this: *J. Mater. Chem. A*, 2026, **14**, 3631

Can solvothermal synthesis drive defectivity and unlock better electrochemical performance in Li-rich layered oxides?

Arcangelo Celeste, *[a] Valeria Lombardi,[abc] Marta Mirolo,[d] Yan Lu,[e] Rafal E. Dunin-Borkowski,[e] Eric Hirschmann, [f] Maik Butterling,[f] Macie O. Liedke,[f] Andreas Wagner, [f] Antonino Santoni,[g] Priscilla Reale,[bg] Maria Assunta Navarra, [a] Sergio Brutti [a] and Laura Silvestri *[b]

Received 4th August 2025
Accepted 26th November 2025

DOI: 10.1039/d5ta06306j

rsc.li/materials-a

This study highlights a novel perspective on the role of defectivity in governing the electrochemical performance of cobalt-free lithium-rich layered oxides (LRLOs), specifically $Li_{1.24}Mn_{0.62}Ni_{0.14}O_2$. By varying the solvent environment during solvothermal synthesis, using binary mixtures of water and ethanol, we demonstrate that the nature of the solvent profoundly influences defect formation within the material. These solvent-dependent defect structures emerge as the key drivers of electrochemical behavior, rather than just crystallinity or composition. Through advanced characterization techniques including synchrotron X-ray diffraction, electron diffraction, transmission electron microscopy, and positron annihilation lifetime spectroscopy, we reveal how each solvent system tailors specific microstructural and defect profiles. Despite identical nominal compositions, these variations in defectivity lead to remarkable different electrochemical performances: higher ethanol content promotes small vacancies and electronic defects, boosting initial capacity but reducing stability, while lower ethanol fractions favour larger vacancies and stacking faults, yielding more balanced performance. Our findings underscore the critical role of solvent selection in tuning defect chemistry, offering a new pathway for optimizing LRLO materials by intentionally controlling defect landscapes during synthesis.

Introduction

Rechargeable batteries offer a practical and sustainable solution to support the growing electric vehicle market and the increasing demand for energy storage systems for renewable energy sources.[1] Among the different rechargeable battery chemistries, Li-ion batteries (LIBs) are the technology with the highest level of maturity, able to temporarily meet this growing demand, thanks to their higher energy and power density compared to other chemistries (*e.g.*, 250 Wh kg^{-1} for LIBs *vs.* 150 Wh kg^{-1} for Na-ion batteries).[2] However, LIBs in their current state represent only a short-term solution due to their intrinsic limitations that include high cost, limited supply of some of their key elements such as lithium or cobalt, and performance limitations.[3]

The performance of LIBs is primarily constrained by the cathode materials, as they play a critical role in determining the energy and power density, cycle life, and overall cost of the battery system.[4–6] Currently, Li-rich layered oxide materials (LRLOs) stand out for their specific capacity (> 250 mAh g^{-1}), high working potential (3.6 V *vs.* Li$^+$/Li), energy density (900 Wh kg^{-1}), and low cost.[7,8] The electrochemical performance of lithium-rich layered oxides (LRLOs) is significantly influenced by the architecture of the cathode active material.[9] However, accurately characterizing this structure remains challenging, further complicated by the intricate behaviour exhibited during battery cycling, ultimately hindering efforts to optimize LRLOs for better performance.[10–12] Regardless of the pristine structural configuration, these materials exhibit instability during cycling due to the oxygen redox reactions, which are however crucial for achieving their high capacity. Specifically, the layered architecture of the LRLOs undergoes transformation into a spinel-like phase. This transition is linked to multiple adverse effects that currently hinder their application in commercial battery systems.[13]

---

[a] *Department of Chemistry, Sapienza University of Rome, P.le Aldo Moro 5, 00185, Rome, Italy. E-mail: arcangelo.celeste@uniroma1.it*
[b] *Department of Energy Technologies and Renewable Sources, ENEA C. R. Casaccia, via Anguillarese 301, 00123, Rome, Italy. E-mail: laura.silvestri@enea.it*
[c] *Material Research Institute (IMFAA), Aalen University, Beethovenstraße 1, 73430, Aalen, Germany*
[d] *ESRF – The European Synchrotron, 71 Avenue des Martyrs, 38000 Grenoble, France*
[e] *Ernst Ruska-Centre for Microscopy and Spectroscopy with Electrons, Forschungszentrum Jülich GmbH, Wilhelm-Johnen-Straße, 52428, Jülich, Germany*
[f] *Helmholtz-Zentrum Dresden-Rossendorf, Bautzner Landstraße 400, 01328, Dresden, Germany*
[g] *Nuclear Department, ENEA C. R. Frascati, via E.Fermi 45, 00044 Frascati, Italy*

To tackle the existing challenges associated with lithium-rich layered oxides, researchers investigated a range of synthesis techniques. These methods influence various material characteristics, including phase crystallinity, purity, particle size, morphology, and ultimately, electrochemical performance.[8,14–17] The synthetic approach can significantly impact the scalability and reproducibility of production processes. Within this framework, the solvothermal method stands out as a highly effective technique for the synthesis of lithium-rich layered oxides (LRLOs), providing the ability to precisely control crystal growth.[18–20] This approach enables the customization of material properties by adjusting various reaction parameters, including reactant concentrations, types of solvents, reaction temperature, and synthesis duration.[21] As an example, Shao *et al.* reported a LRLO material synthesized *via* a multi-solvent solvothermal method, showing how the solvent plays a crucial role in the precipitation rate of the transition metals (TMs) and obtaining a 3D porous structure and uniform particle size.[22] Moreover, Yan *et al.* showed that the chemical–physical properties of the final material are also strongly influenced by the precipitators.[23]

In this study, we illustrate that modifications to the crystallization environment significantly influence the crystal structures and defect formations (including vacancies, antisites, small voids, large voids, stacking faults, and twin boundaries) within lithium-rich layered oxides (LRLOs). These alterations consequently affect the reversibility of lithium-ion intercalation/deintercalation into the cathode structure. To investigate this, we examine the impact of various crystallization media, specifically five different liquid mixtures of ethanol and water at varying volume ratios, on the structural, morphological, and electrochemical properties of a cobalt-free Li-rich layered oxide, namely $Li_{1.24}Mn_{0.62}Ni_{0.14}O_2$, synthesized *via* a solvothermal method.[24] Our findings reveal that the crystallization medium critically governs the defect chemistry and, consequently, the electrochemical response of $Li_{1.24}Mn_{0.62}Ni_{0.14}O_2$. For these solvent mixtures, samples prepared with higher ethanol content tend to develop a higher density of small vacancy clusters and more pronounced electronic defects, which correlate with enhanced initial capacity but lower coulombic efficiency and reduced capacity retention. Conversely, samples synthesized with a lower amount of ethanol feature favourable surface chemistry and a defect structure that supports balanced electrochemical performance, leading to good capacity, improved efficiency, and superior cycling stability.

Materials and methods

Sample preparation

Lithium acetate ($LiCH_3COO\cdot 2H_2O$), nickel(II) acetate ($Ni(CH_3COO)_2\cdot 4H_2O$), manganese(II) acetate ($Mn(CH_3COO)_2\cdot 4H_2O$), oxalic acid ($C_2H_2O_4$) and absolute ethanol (C_2H_6O) were purchased from Sigma-Aldrich and used as received. Five different reaction solvents were prepared by adding ultrapure water (Milli Q) and absolute ethanol according to the following proportions $H_2O : EtOH = 1 : 0$, $2 : 1$, $1 : 1$, $1 : 2$ and $0 : 1$ v/v. Before solvothermal treatment, two solutions were prepared as follows:

- Sol. A: prepared by dissolving into the reaction solvent a mixture of lithium (with an additional 5% atomic excess to compensate for any evaporative losses during the thermal treatment at high temperature), nickel and manganese acetates in stoichiometric amounts.
- Sol. B: 1 M solution of oxalic acid (prepared using the same solvent of Sol. A), acting as a chelating and precipitant agent. The amount of oxalic acid was chosen in order to have a molar ratio of Ox.Ac. : (Mn + Ni) of 1 : 1.5.

The two solutions were properly mixed and poured in a Teflon-lined autoclave for the solvothermal synthesis, carried out at 180 °C for 12 h. At the end of solvothermal treatment the reactor was cooled down to room temperature, then the obtained product was recovered, and the solvent evaporated. The as-obtained reaction precursor was dried overnight in an oven at 80 °C under vacuum and successively subjected to the final thermal treatment in a muffle furnace in an air atmosphere. The thermal procedure consisted of a first step at 450 °C for 2 h (10 °C min^{-1}), and a second step at 900 °C for 12 h (10 °C min^{-1}).

Chemical–physical characterization

The oxalate intermediate phases were analysed by using a Rigaku SmartLab diffractometer using a Cu Kα radiation source.

High-resolution X-ray powder diffraction data were acquired at the ID22 beamline of the ESRF synchrotron radiation source (Grenoble, France), using an energy of 35 keV (corresponding to a wavelength of 0.354 Å), and the setup equipped with crystal analyzers, with a 2θ resolution of 0.003°.[25,26] Diffraction patterns were analysed by Rietveld refinement using the software FAULTS.[27]

Attenuated total reflectance Fourier transform infrared spectroscopy measurements (ATR-FTIR) were performed with an Agilent Cary 630 instrument.

Raman spectroscopy measurements were carried out on a Dilor Labram instrument equipped with a He–Ne laser source at 632.7 nm and a CCD cooled detector.

X-Ray photoemission spectra (XPS) were acquired using a PSP TSX-400 non-monochromatized photon source operating at 1253.6 eV (Mg K_α) and a PREVAC EA15 electron spectrometer in an ultra-high-vacuum chamber with a base pressure of about 5×10^{-10} mbar. Core-level photoemission data were recorded at 50 eV pass energy and 0.1 eV step. The spectra were fitted using the CASA XPS software with a Shirley-type background and pseudo-Voigt line-shapes.

A Zeiss Auriga field-emission high-resolution scanning electron microscope equipped with an energy-dispersive X-ray (EDX) spectroscopy system was used to acquire SEM micrographs. Precursor SEM micrographs were acquired using a Phenom ProX Desktop SEM.

Variable energy positron annihilation lifetime spectroscopy (VEPALS) measurements were conducted at the Mono-energetic Positron Source (MePS) beamline at HZDR, Germany.[28] A CeBr3 scintillator detector coupled to a Hamamatsu R13089-100 photomultiplier tube (PMT) was utilized for gamma photon detection. The signals were processed using the Teledyne SP Devices ADQ14DC-2X digitizer (14-bit vertical resolution and 2 GS per s horizontal resolution).[29] The overall time resolution of the measurement system is ≈0.250 ns and all spectra contained at least 10^7 counts. A typical lifetime spectrum $N(t)$, the absolute value of the time derivative of the positron decay spectrum, is described by

$$N(t) = R(t) \times \sum_{i=1}^{k+1} \frac{I_i}{\tau_i} e^{\frac{-t}{\tau_i}} + \mathrm{BG}$$

where k is the number of different defect types contributing to positron trapping, which are related to $k + 1$ components in the spectra with the individual lifetimes τ_i and intensities I_i ($\Sigma I_i = 1$).[30] The instrument resolution function $R(t)$ is a sum of two Gaussian functions with distinct intensities and relative shifts both depending on the positron implantation energy, E_p. It was determined by the measurement and analysis of a reference sample, *i.e.* amorphous Yttria-stabilized zirconia (YSZ), which exhibited a single lifetime component. The background (BG) was negligible, hence fixed to zero. All spectra were deconvoluted using a non-linear least-squares fitting method, minimized by the Levenberg–Marquardt algorithm, employed within the fitting software package PALSfit.[31] In general, the positron lifetime increases with defect size and open volume size. The positron lifetime and its intensity have been probed as a function of positron implantation energy E_p which was recalculated to the mean implantation depth $\langle z \rangle$, using the Makhovian profile and average values of the parameters m and n.[32]

The microstructure and selected area electron diffraction (SAED) analyses of the samples were performed on an FEI Titan 80–300 TEM with an accelerating voltage of 300 kV.

Electrode preparation and cell assembly

Electrodes were prepared in a dry room with a dew point of −70 °C and at 20 °C, mixing 80 wt% active material, 10 wt% SuperP carbon and 10 wt% polyvinylidene fluoride (PVdF) with the addition of *N*-methyl 2-pyrrolidinone (NMP) to obtain a slurry. The slurry was spread out onto an aluminium foil by using a doctor blade with a thickness of 200 µm. The obtained film was dried in oven at 60 °C under vacuum until the solvent evaporated, then disks of 10 mm of diameter were cut and dried overnight in a Büchi oven at 110 °C under vacuum. The dried electrodes were then transferred to an Argon filled glovebox (Jacomex GP(Concept) with the O_2 and H_2O level below 0.5 ppm), where the electrochemical cells were assembled. Al-coated coin cells (type CR2032) were used to study the electrochemical properties of $Li_{1.24}Mn_{0.62}Ni_{0.14}O_2$-based electrodes. The cell was assembled using the as prepared electrodes as the working electrode, metallic lithium as the counter electrode and LP30 (1 M $LiPF_6$ in ethylene carbonate (EC) : dimethyl carbonate (DMC) = 1 : 1 v/v) as the aprotic electrolyte-soaked Whatman GF/D separator.

Electrochemical tests

Galvanostatic cycling was performed using a Maccor battery test system (S4000) in the voltage range of 2.0–4.8 V, at different scan rates (1C = 380 mA g^{-1}). To stabilize the cathode electrolyte interphase and prevent the consumption of electrolyte and lithium ions, a formation procedure has been applied to the cells before any charge/discharge test, according to ref. 33. The procedure consisted of 2 charge/discharge cycles at C/10, 2 charge/discharge cycles at C/5 and 2 charge/discharge cycles at 1C. At the end of all the charge steps, a potentiostatic step at 4.8 V (with a current cutoff of C/20) has been applied, while a rest of 1 h has been applied before changing the C-rate. Formation cycles obtained before the galvanostatic cycling test at C/10 for all the samples have been reported in Fig. S1. Cyclic voltammetry tests were carried out on a Biologic VMP-3e potentiostat between 2.0 and 4.8 V at different scan-rates (from 0.05 mV s^{-1} to 0.7 mV s^{-1}). All the electrochemical tests have been conducted in a climate chamber at 30 °C.

Results and discussion

Sample composition and labelling

The influence of synthesis conditions on the chemical–physical and electrochemical properties of cobalt-free Li-rich materials, specifically $Li_{1.24}Mn_{0.62}Ni_{0.14}O_2$, is examined by varying the reaction solvent during the solvothermal treatment. Notably, water and ethanol are chosen for this study, utilized both as pure solvents and in various mixtures, due to their unique physical properties.[34] Previous studies[35,36] emphasize that the incorporation of ethanol, a solvent with a lower dielectric constant than water, can enhance nucleation kinetics and modify the crystal growth processes of the resulting particles. Additionally, ethanol's complete miscibility in water allows for the creation of mixtures in any desired composition. However, the properties of the resulting water–ethanol binary solutions exhibit anomalous characteristics when compared to those of the pure solvents, as the intermolecular interactions change in a non-linear manner during the gradual dissolution of ethanol in water.[36]

In this study, we synthesized five distinct samples, each labelled according to the respective water (W) and ethanol (E) content in the solvothermal reaction bath, as summarized in Table 1. The compositions of all the samples after the solvothermal synthesis and the high temperature annealing have been analysed using ICP-OES, and the results closely match the expected nominal stoichiometric values calculated from the reagents (Table 1).

Assessment of the synthesis route: the oxalate intermediates

Fig. 1 shows all X-ray diffraction (XRD) patterns, ATR-FTIR spectra, and SEM images for materials collected at an intermediate stage of the synthesis, after the solvothermal treatment in an autoclave for 12 h at 180 °C, but before high temperature annealing. For the sake of clarity, these synthesis intermediates have been labelled following the same coding used for the final synthesis products (see Table 1), with the addition of a P-prefix.

Table 1 Label adopted for the $Li_{1.24}Mn_{0.62}Ni_{0.14}O_2$ samples and composition calculated by ICP-OES

	Reaction solvent v/v ratio		Experimental composition (ICP-OES)		
Sample name	Water	Ethanol	Li	Mn	Ni
W_1	1	0	1.267 ± 0.005	0.618 ± 0.001	0.115 ± 0.001
W_2E_1	2	1	1.262 ± 0.002	0.631 ± 0.001	0.107 ± 0.001
W_1E_1	1	1	1.262 ± 0.002	0.624 ± 0.005	0.114 ± 0.001
W_1E_2	1	2	1.281 ± 0.001	0.618 ± 0.004	0.101 ± 0.003
E_1	0	1	1.288 ± 0.005	0.603 ± 0.001	0.109 ± 0.004

The XRD pattern of the P-W_1 sample exhibits characteristic peaks of $MnC_2O_4\cdot 2H_2O$, $NiC_2O_4\cdot 2H_2O$, and $Li_2C_2O_4$, as expected using oxalic acid as a precipitating agent (see Fig. 1a and S1).

As ethanol concentration in the reaction environment increases, the diffraction patterns evolve. In the case of the P-E_1 sample, the diffraction peaks can be attributed to anhydrous MnC_2O_4, anhydrous NiC_2O_4, and $Li_2C_2O_4$. The diffractograms between the two extremes exhibit intermediate features, with a transition marked by the disappearance of the peak around 18°, which is primarily associated with $MnC_2O_4\cdot 2H_2O$, and the appearance of new peaks around 24°, corresponding to NiC_2O_4. The ATR-FTIR spectra confirm the XRD findings (Fig. 1b). Strong peaks in the range of 1800 to 1100 cm^{-1} are observed, attributed to the asymmetric stretching ν_{as}(C–O), symmetric stretching ν_s(C–O), and bending δ(OCO) vibrations of all metal oxalates. Although there are slight changes in the relative intensities of these peaks, they remain evident throughout the series. In the P-W_1 sample, the vibrational analysis additionally reveals a pronounced and well-defined stretching vibration of water ν(OH) around 3300 cm^{-1}, whose intensity decreases for the samples where the water is partially or completely replaced with ethanol, reinforcing the observations made from the XRD patterns. Furthermore, significant differences in the morphologies of the precursors are observed, as shown in Fig. 1c. The P-W_1 sample displays irregular particles with no preferential growth. As the ethanol content in the reaction solvent increases, rod-like structures become increasingly prominent, especially in the P-W_1E_2 sample. In contrast, the precursor obtained in pure ethanol exhibits particles with flake morphology. These observations underline the impact of solvent variation on the

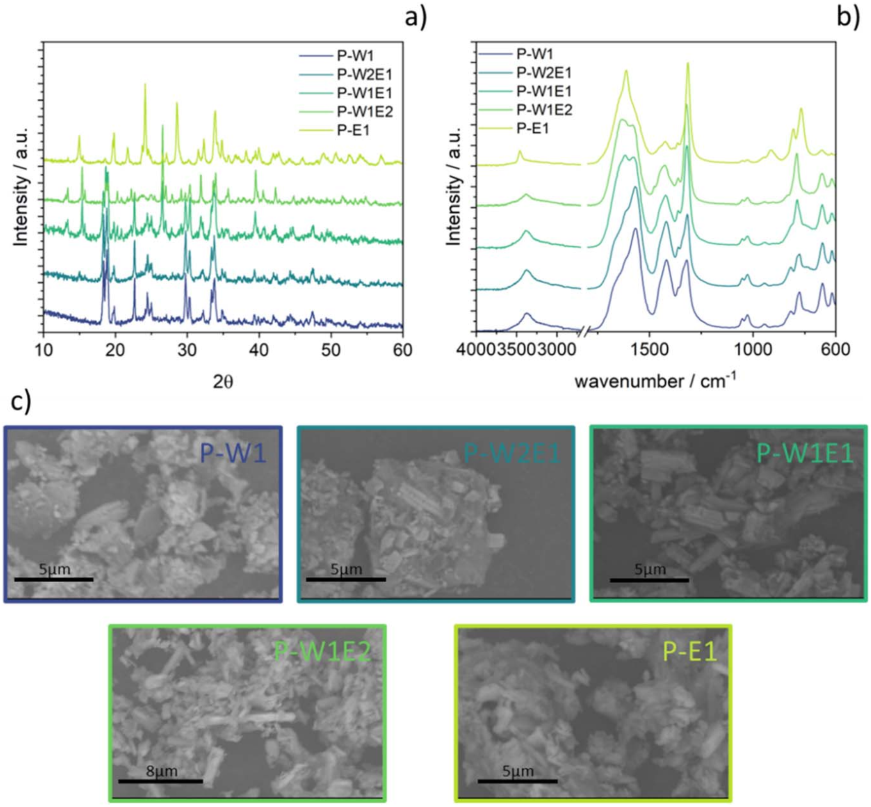

Fig. 1 (a) Diffraction patterns acquired with a Rigaku SmartLab, (b) ATR-FTIR spectra and (c) SEM images of the precursor samples, recovered at the end of solvothermal treatment.

solubility of the reactants, metal solvation and the subsequent nucleation and crystal growth processes.[37] Indeed, the dielectric constant, excess volume, and vapor pressure of ethanol/water mixtures can provide valuable insights into the interactions occurring during the synthesis of the precursors.[38,39] The dielectric constant of a solvent influences the solvation dynamics and the interactions between the metal precursors and the solvent molecules. As reported in the literature,[40–42] the dielectric constant of ethanol is significantly lower than that of water, which affects the ionization and solvation of the ions during the synthesis process. This difference can lead to variations in the structural properties of the precursors, as the solvation environment directly impacts the nucleation and growth of the crystalline phases. Moreover, the mixtures exhibit pronounced deviations from ideality with respect to the pure solvents, water and ethanol. This is clearly reflected in the excess volume of ethanol–water mixtures, which serves as a reliable indicator of the non-ideal intermolecular interactions.[42,43] Negative excess volumes suggest strong interactions between ethanol and water molecules, more than in the pure solvent, which can enhance the precipitation rate of transition metals during solvothermal synthesis. This can result in differences in the morphology and particle size of the precursors, as observed in the various solvent compositions used in the study, as well as in the different micro-defectivity of the products (see below). In the solvothermal method, the vapor pressure of the solvent mixture also plays a crucial role in the synthesis process. Higher pressures can accelerate crystal growth along preferential directions due to changes in kinetic conditions.[44] The experimental data indicate that the vapor pressure of the ethanol/water mixture decreases with increasing ethanol concentration, which can influence the crystallization kinetics and the final properties of the Li-rich layered oxides.[45] In addition, consistent with previous studies on layered oxides,[46] the solvent environment and oxygen chemical potential influence surface energies and defect formation, further modulating precursor morphology. These combined effects of solvent composition may help to explain the observed variations in precursor morphology and defectivity, underscoring the critical role of solvent choice in tailoring material synthesis outcomes. Furthermore, the non-ideal interactions between water and ethanol solvents lead to unpredictable precursors in terms of morphology and defectivity.[37] It should be noted that no linear correlation is expected between the investigated parameters and the solvent composition. This is because the chemical–physical properties of mixed solvents differ significantly from those of the corresponding pure solvents. Consequently, the behaviour of the system cannot be interpreted as a simple interpolation of the pure solvent data.

Assessment of the synthesis route: the LRLO products

The final crystallization of the LRLO lattices has been obtained by annealing the corresponding precursors in a furnace at 900 °C for 12 hours in air. As shown in Fig. S2, the morphologies of the precursors are not retained in the samples. In fact, the high temperature procedure resulted in the formation of nanoparticles exhibiting a quasi-spherical shape with a dimension of about 200–300 nm for all samples. Turning to the crystal structure analysis, the X-ray diffraction (XRD) patterns illustrated in Fig. 2a reveal the distinctive diffractograms of lithium-rich layered oxides (LRLOs), indicating that the expected phase has been successfully synthesized across all solvent compositions.[9,24] To gain deeper insights into the structural attributes of these samples, Rietveld refinement was conducted on the diffraction patterns utilizing the FAULTS software, as depicted in Fig. S3 and detailed in Table S1, thereby elucidating critical information regarding the crystallographic cell parameters. The XRD patterns were analysed using the *C*2/*m* space group in which the structure is described as a stack of atomic layers. Table S2 presents the refined cell parameters, indicating only slight variations among the different samples. However, as summarized in the scheme reported in Fig. 2b, the composition of the solvent primarily affects the microstructure and defect formation, rather than the phase stability. In fact, high-resolution XRD analysis confirmed the exclusive formation of the layered phase, with no detectable secondary phases. The extent

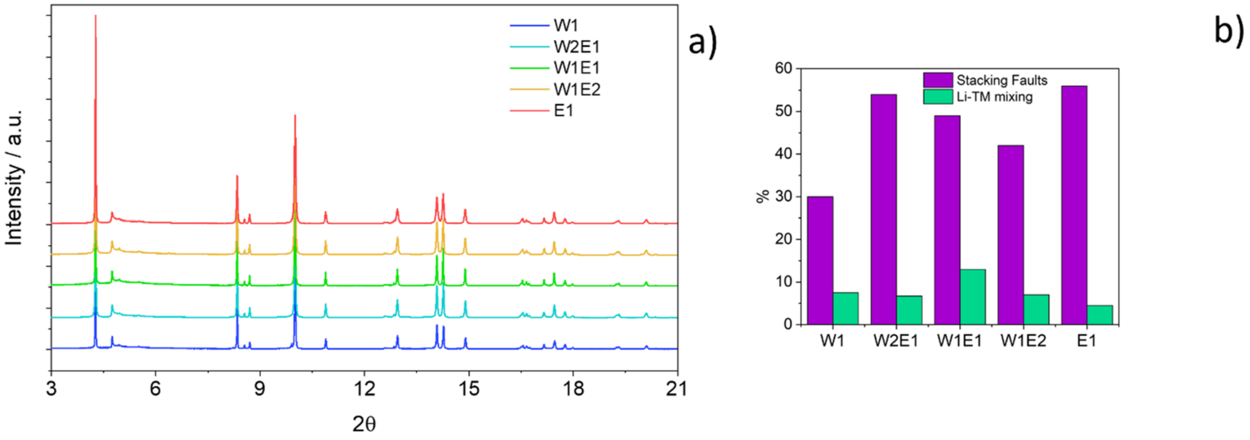

Fig. 2 Comparison of (a) diffraction patterns acquired at the ESRF synchrotron radiation source using an energy of 35 keV and (b) stacking faults and Li-TM percentages.

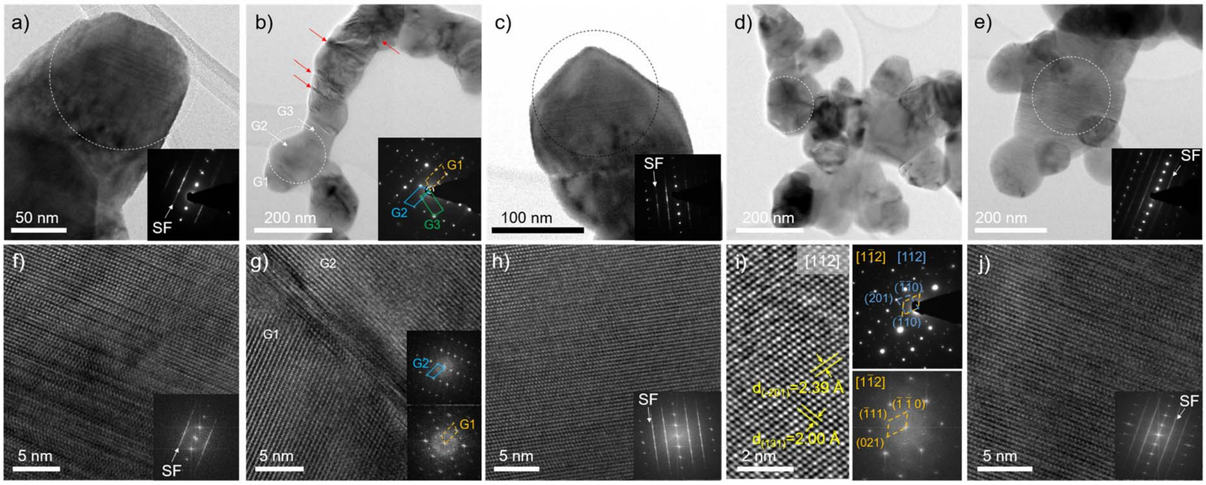

Fig. 3 (a–e) Bright field TEM images of W1, W2E1, W1E1, W1E2, and E1, respectively. The SAED patterns of the dashed circle areas in each image are shown in their lower right. SFs are clearly demonstrated by both TEM images and SAED patterns in a, c and e. (b) Parallel coincidence boundaries shown by red arrows and twin grains (G1 and G2). (f–j) HRTEM images of each circled area, showing obvious SFs in f, h and j, and twin boundaries in g. (i) The interplanar spacing in the HRTEM image and indexes in SAED patterns and Fourier transform demonstrate the *C*2/*m* Li_2MnO_3 prototype crystal structure.

of stacking faults varies significantly with the solvent: considering the pure solvents, it is lowest in the water-based system and highest in the ethanol-based one. This trend is likely due to the faster reaction kinetics associated with ethanol (lower dielectric constant), which promotes the formation of a more defective layered structure. Specifically, the stacking fault degree was found to be 30% for the W_1 sample and 56% for the E_1 sample. In systems using mixed solvents, different behaviour can be seen due to the unique properties of the mixtures. Due to strong intermolecular interactions between ethanol and water molecules in the investigated mixtures and the formation of a more compact packing, the stacking fault density increases notably with the initial addition of ethanol to water but then decreases as the ethanol content continues to rise. For instance, samples prepared with water/ethanol mixtures showed intermediate stacking fault values, ranging from 42% to 54%. Interestingly, the degree of Li-TM mixing also varies across the samples and generally exhibits an inverse correlation with the stacking fault density, although the W_1E_1 sample deviates from this trend.

Further structural characterization was carried out with TEM and Fig. 3 shows the cryptographic microstructure of all the samples. Fig. 3a–e show the bright field TEM images of W_1, W_2E_1, W_1E_1, W_1E_2, and E_1, respectively. The SAED patterns of the circle areas are displayed in the lower right corner. Fig. 3f–j show the corresponding high-resolution TEM (HRTEM) images from the selected grains. Same as FAULTS analysis, frequent stacking faults (SFs) are shown in Fig. 3a, c and e and correspondingly in Fig. 3f, h and j. In the upper panels, low magnification TEM images display parallel line contrast which exhibit SF contrasts, and the corresponding SAED patterns demonstrate typical SF features. In addition to SFs, coincidence boundaries and twins were found in sample W_2E_1, as shown in Fig. 3b and g. The SAED pattern includes two boundaries, among which grain 1 (G1) and G2 are twins, and G2 and G3 share the same plane as the boundary. The red arrows indicate the other coincidence boundaries. Such boundaries are planar defects which are similar to SFs. Fig. 3g displays the HRTEM images of G1 and G2. The Fourier transform of G1 and G2 is consistent with SAED, showing a twin boundary. TEM characterization of the sample of W_1E_2 is shown in Fig. 3d and i. In particular, the crystal structure is revealed by the HRTEM image and SAED pattern taken from the circled area, shown in Fig. 3d. The indexes in SAED indicated by yellow and blue labels present zone axes of $[1\bar{1}2]$ and [112] of the C2/m Li_2MnO_3 prototype,

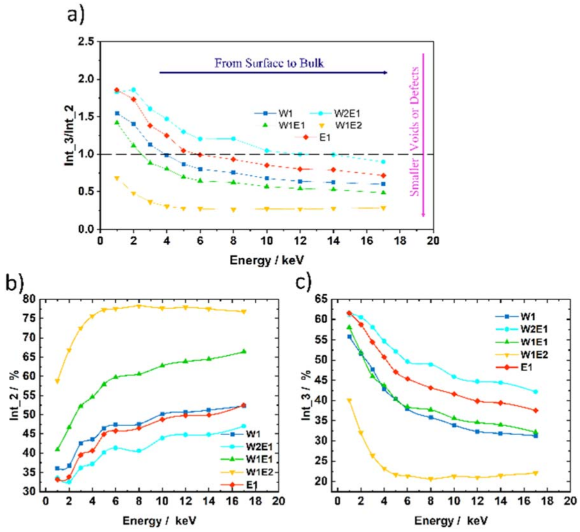

Fig. 4 (a) Ratio of intensity values (Int3/Int2) of Tau2 and Tau3 lifetime components and intensity values of Tau2 (b) and Tau3 (c) lifetime components from PAL spectroscopy, as a function of energy for the different samples.

respectively. The HRTEM image is taken along the $[1\bar{1}2]$ zone axis, and the interplanar spacing of (131) and $(\bar{2}01)$ is 2.00 Å and 2.39 Å, respectively. The corresponding Fourier transform is shown in the lower right which is consistent with the yellow labels in the SAED pattern. Positron lifetime spectroscopy was employed to investigate the vacancy-related defects in the five samples: W_1, W_2E_1, W_1E_1, W_1E_2, and E_1 (see Fig. 4). The measurements revealed up to three major lifetime components (Tau1–Tau2–Tau3) and two additional long-lifetime components (Tau4–Tau5), with corresponding intensity values (Int1–Int2–Int3–Int4–Int5). Due to their minimal contribution to the total signal (Int4 + Int5 < 2%) and their likely association with surface effects, Tau4 and Tau5 are excluded from further discussion (Fig. S4a and b).

All observed lifetimes exhibited only minimal dependency on the implantation profile, indicating that the defect structures are relatively stable across the investigated energy range. Tau1 was observed exclusively in samples W_1 (94 ps), E_1 (75 ps), and W_2E_1 (75 ps), with an intensity of ∼10% (Fig. S4c). This suggests a reduced bulk lifetime, which is indicative of the onset of defect saturation. To validate this observation, ATSUP GC scheme simulations were conducted, predicting a bulk lifetime of 153 ps for a defect-free material. However, this value could not be consistently fitted across the entire sample set, reinforcing the notion of defect-related modifications in the bulk material. A consistent Tau2 value of approximately 220 ps was found in all samples. According to simulation results, this lifetime corresponds to the presence of small vacancy clusters consisting of 3 to 4 missing atoms. Tau3 was found at approximately 415 ps across all samples, which is characteristic of large vacancy clusters or voids containing more than 15 missing atoms. Despite the uniformity in lifetime, the intensity of this component (Int3) varied significantly among the samples, reflecting differences in defect concentration and structural homogeneity. Unlike the positron lifetime values, the intensity of the observed lifetimes exhibited notable variations among the different samples and implantation energies. The two different vacancy clusters correspond to the lack of small groups of bonded atoms, with a different void size, in the material structure and likely originate from an uneven crystallization of the lattices during the synthesis. Under the assumption of electroneutral voids, one may speculate that the smallest vacancies (*i.e.*, 3–4 atoms) possibly imply the lack of Li_2O, NiO or MnO_2 units, with +1, +2, +4 and −2 being the mean oxidation states of Li, Ni, Mn, and O, respectively. Under the same assumption, the large voids (*i.e.*, >15 atoms) may be explained by the missing crystallization within the structure of approximately one whole unit cell (*i.e.*, 12 atoms). Considering the pure solvents, the intensity of larger voids (Int3) decreases from the surface to the bulk for both, but the sample synthesized in ethanol shows a bigger intensity across all the energies (see Fig. 4), again likely due to the faster nucleation compared to water. In contrast, the intensity of smaller voids (Int2) is comparable. This suggests that the ethanol solvent promoted the formation of larger vacancy clusters, potentially due to differences in reaction kinetics and crystallization during synthesis. For the mixed solvent systems, the behaviour was more complex, and the intensity trend of large vacancy-clusters followed the order: $W_1E_2 < W_1E_1 < W_2E_1$, as reported in Fig. 4. Sample W_1E_2 exhibited the lowest intensity for large vacancy clusters (Int3), suggesting a more homogeneous structure compared to the other samples. In contrast, W_2E_1 showed the highest intensity for large vacancy clusters, indicating a higher concentration of large voids or defects. The rich complexity of the vacancy clusters in the various samples can be outlined by reporting the trend of the ratio between the intensities of the Int3 and Int2 components as a function of the implantation energies as shown in Fig. 4. When this ratio is above 1, the concentration of the large voids (∼415 ps, component 3) is larger than the concentration of the small vacancy clusters (∼220 ps, component 2) and *vice versa* in the case Int3/Int2 < 1. Overall, the Int3/Int2 ratio suggests remarkable structural differences in the defectivities among samples. In particular, W_1E_2 shows at any implantation energy (*i.e.*, implantation depth) the least number of large voids, and thus the largest amount of small cluster vacancies, whereas W_2E_1 exhibits the highest concentration of large voids and the smallest of the small cluster vacancies. These findings confirm the trend observed with the XRD analysis, in particular with the stacking faults. XPS analysis was performed to characterize the surface of the different layered oxides prepared in the different solvothermal environments.

Fig. 5a and b show the XPS core-level spectrum of Ni $2p_{3/2}$ and Mn $2p_{3/2}$, respectively. The binding energies are corrected with the C 1s C–C(C–H) peak set at 284.8 eV. The interpretation and quantification of the Ni $2p_{3/2}$ signals are known to carry a high degree of uncertainty due to the complex, extended multiplet, shake-up and plasmon loss structures, further confounded by the overlap between various chemical states. Due to the broad shape of the peak and the absence of visible structures, a simple fitting strategy has been adopted in this work to individuate the peak position, by using an asymmetric line-shape and including the plasmon peak in the fitting procedure. For all the samples, the position of the Ni $2p_{3/2}$ peak is around 855.1 ± 0.1 eV, a binding energy in good agreement with D. P. Abraham[47] and coherent with Ni(II). The Mn $2p_{3/2}$ signals are in the 642–644 eV region of binding energies. To fit

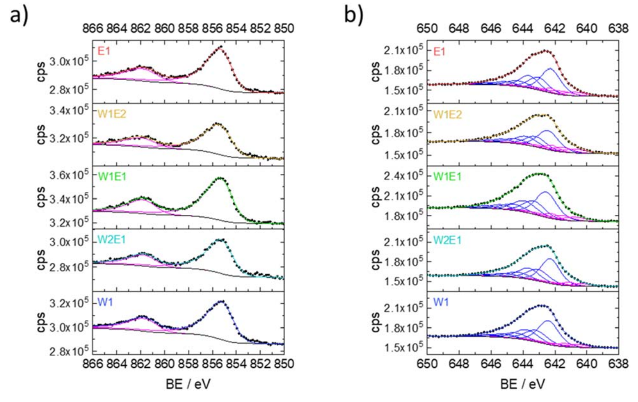

Fig. 5 XPS spectral reconstruction for the core-level spectra of (a) Ni $2p_{3/2}$ and (b) Mn $2p_{3/2}$.

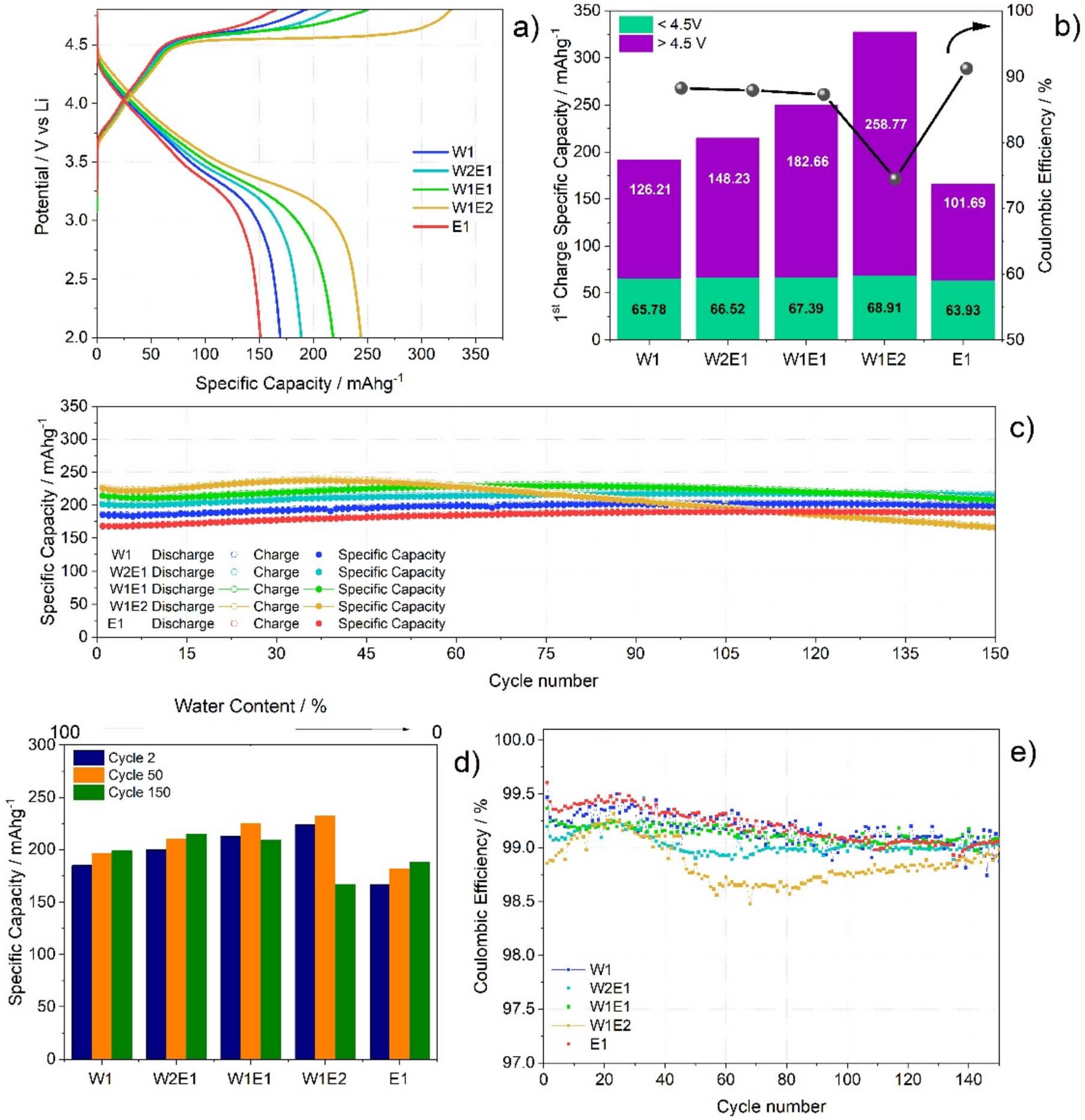

Fig. 6 (a) First cycle potential profile, (b) specific capacity values obtained during the first charge process and coulombic efficiency of the first cycle, (c) discharge specific capacity *vs.* cycle number obtained after the formation procedure, (d) summary of specific capacity obtained after 2, 50 and 150 cycles as a function of water content in the reaction solvent and (e) coulombic efficiency, obtained with galvanostatic cycling in the voltage range between 2 and 4.8 V at C/10.

them, multiple splitting of multiple oxidation states has been taken in consideration. Mn(III) and Mn(IV) fit parameters as proposed by Ilton[48] were fixed for individual oxidation states but allowed to shift in energies and intensities as packets relative to other oxidation states. An allowance for relative BE shifts acknowledges the possibility that the ionicity/covalency and Madelung potential are different in multivalent compared to monovalent minerals, or in different structures. The best fit to the layered Mn $2p_{3/2}$ spectrum yielded almost 80% Mn(IV) and 20% Mn(III), for an average oxidation state of 3.8, with small variations between samples (*i.e.* W_1 +3.84, W_2E_1 +3.85, W_1E_1 +3.80, W_1E_2 +3.75, E_1 +3.79, for the mean oxidation state of the Mn ions in the LRLO structures). Generally, a lower oxidation state than 4 for Mn indicates a more defective surface. In the case of pure solvents, the E_1 sample shows a lower oxidation state compared to W_1, suggesting a more defective material, which is consistent with findings from other techniques. Similarly, for the mixtures, a higher concentration of defects correlates with a lower Mn oxidation state. The variability of relative amount of each of these defects for different synthetic conditions confirms the remarkable impact of the solvothermal media on the precipitation thermodynamics/kinetics and therefore on the periodicity/crystallinity of the resulting lattice.

Although the XPS spectra of the samples are very similar with only subtle differences, all fitting parameters are provided in Table S3 of the SI. The small variations fall within typical experimental uncertainty and agree with literature values,[48] indicating subtle changes in the local chemical environment rather than significant oxidation state shifts. The relatively broad peaks arise from the higher pass energy employed to improve signal intensity.

Electrochemical performance in lithium half-cells

To investigate the influence of the reaction solvent on the electrochemical performance of the synthesized Co-free LRLOs, galvanostatic cycling tests were conducted in lithium half-cells at a current density of 38 mA g^{-1} (C/10) within a voltage window of 2.0–4.8 V. The results reveal significant insights into the relationship between electrochemical behaviour, structural defects, and surface chemistry. The electrochemical behaviour of LRLOs is notably sensitive to minor variations in synthesis parameters, which manifest in the first charge capacity and cycling stability (Fig. 6a and b). The first charge process typically proceeds *via* a two-step mechanism as shown in Fig. 6a: a slope between 3.5 V and 4.5 V associated with the oxidation of transition metals and a plateau above 4.5 V attributed to the oxygen redox reaction (Fig. 6c–d). For all samples, an increase in capacity was observed during the first 30 cycles, with W_1E_2 reaching nearly 230 mAh g^{-1} at cycle 45. However, after 50 cycles, performance stabilization was observed for W_1 and W_2E_1, while W_1E_2 exhibited significant degradation, retaining only 66% of its initial capacity after 150 cycles. The potential transition from a layered to a spinel-like phase,[8] particularly evident in W_1E_2 (see potential profiles for selected cycles in Fig. S5), is associated with lower coulombic efficiency and rapid capacity degradation (Fig. 6e). The increased defect density likely contributes to structural instability during cycling, leading to more pronounced degradation of electrochemical performance. Indeed, for the mixtures, the capacity retention and electrochemical stability follow the trend: $W_2E_1 > W_1E_1 > W_1E_2$, matching the trend of smaller voids. Moreover, XPS analysis indicated a higher oxidation state of manganese in W_2E_1, suggesting a more stable surface chemistry that correlates with reduced defectivity and improved cycling stability, compared to W_1E_1 and, in particular, W_1E_2.

These results were also confirmed by analysing the behaviour of the samples at elevated C-rate. As shown in Fig. 7a, W_1E_2 retains a high capacity of about 160 mAh g^{-1} at 2C, while for the other samples, it ranges between 100 mAh g^{-1} for W_1E_1 and 120 mAh g^{-1} for W_2E_1 (Fig. 7b).

The cycling stability at 1C is illustrated in Fig. 7c and Fig. S7, where the trend is similar to that already observed at C/10. The initial specific capacity increases progressively from W_1, at approximately 120 mAh g^{-1}, to W_1E_2, which reaches 170 mAh g^{-1}. However, while W_1 and E_1 retain 99 and 102 mAh g^{-1} after 250 cycles, corresponding to capacity retentions of 82% and 85% (Fig. 7d), respectively, W_1E_2 experiences significant fading, retaining only 108 mAh g^{-1} (67% of its initial capacity). In contrast, W_1E_1 and W_2E_1 achieve a more favourable balance, retaining 121 and 120 mAh g^{-1} after 250 cycles (Fig. S8), which corresponds to capacity retentions of 81% and 84%, respectively. Coulombic efficiency (CE) further emphasizes the differences among the electrodes (Fig. S9). W_1E_1 and W_2E_1 sustain efficiencies above 99.5% throughout cycling, indicative of highly reversible Li$^+$ insertion/de-insertion and minimal parasitic reactions. W_1 and E_1 display slightly lower CE values, just below 99.5%, whereas W_1E_2 exhibits a gradual decline to approximately 99% by the 250th cycle. Overall, W_1E_2 exhibits the highest initial capacity and superior rate performance, which can be attributed to its relatively low stacking fault

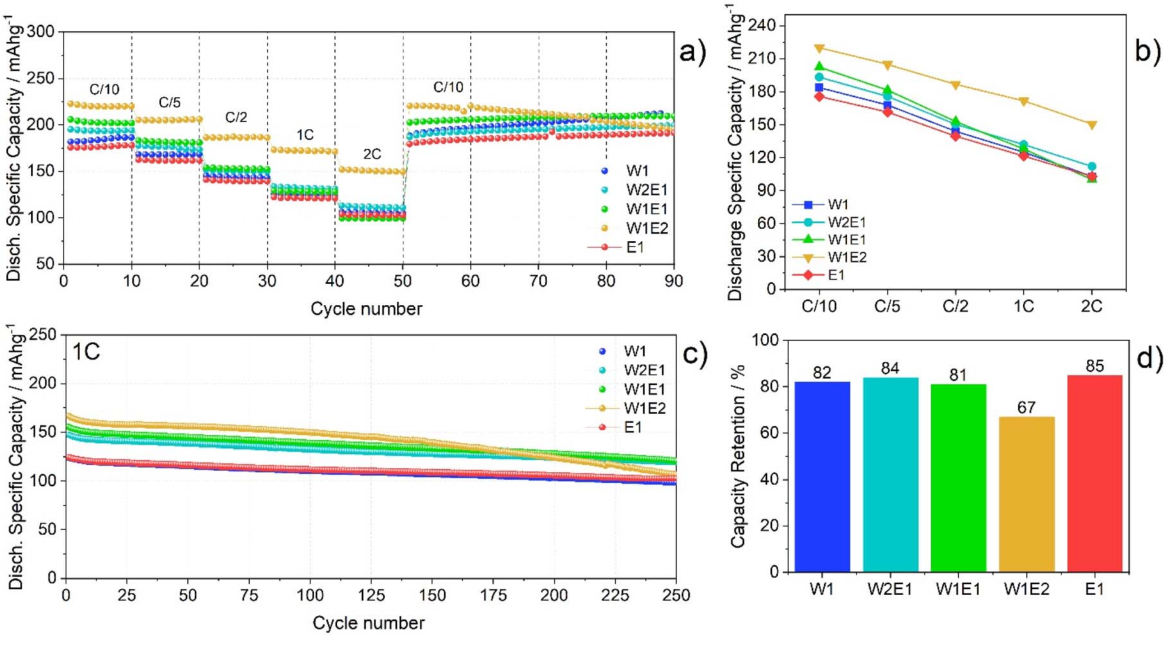

Fig. 7 (a) Rate capability, (b) discharge specific capacity as a function of C-rate, (c) cycling performance at 1C and (d) capacity retention calculated after 250 cycles, obtained by galvanostatic cycling in lithium half-cells.

density, facilitating Li-ion diffusion, and pronounced Li-TM mixing. However, these same structural features, together with the same defects can create highly reactive sites that promote undesirable side reactions, such as the decomposition of the electrolyte (with the observed reduced coulombic efficiency), which consumes active lithium ions and reduces capacity over time. Furthermore, defects (often oxygen vacancies) can lead to the dissolution of transition metal ions into the electrolyte, further degrading the material and causing capacity fade and reduce lattice stability during prolonged cycling. Consequently, W_1E_2 exhibits pronounced capacity fading and a gradual decrease in coulombic efficiency after 250 cycles. In conclusion, galvanostatic cycling tests indicate that the electrochemical behaviour of the samples is closely linked to structural defectivity and surface chemistry, both of which are influenced by the synthesis solvent.

Conclusion

In this study, we systematically investigate the role of solvent composition in the solvothermal synthesis of cobalt-free Li-rich layered oxides (LRLOs) with nominal composition, $Li_{1.24}Mn_{0.62}Ni_{0.14}O_2$.

The solvent composition is a key factor in shaping the morphology and microstructure of the solvothermal precursors, primarily through its impact on ion solvation and nucleation kinetics. However, it is important to note that although the solvent influences both the precursor morphology and defect formation in the final products, these processes occur through different mechanisms. The high-temperature annealing at 900 °C induces significant structural and morphological changes, causing the original shape of the precursors to be lost. Instead, the solvent's role during the annealing process affects defect formation, which ultimately results in variations in the stacking fault density observed in the final cathode materials.

Although a layered phase is formed consistently across all conditions, structural characterization *via* XRD, HR-TEM, and PALS reveals that variations in the water-to-ethanol ratio significantly affect microstructural features and defect density. These structural differences translate directly into electrochemical behaviour, as summarized in Fig. S10. For instance, the ethanol solvent promotes the formation of stacking faults and vacancy clusters, while the binary water–ethanol mixture at a 1 : 2 volume ratio (W_1E_2) yields the smallest stacking fault density and a marked reduction in large defects, suggesting an increased concentration of smaller defects. Galvanostatic cycling in lithium half-cells shows that the W_1E_2 sample delivers the highest initial discharge capacity (330 mAh g^{-1} at C/10), likely due to enhanced participation of oxygen redox processes. However, it also showed lower coulombic efficiency and faster capacity fading during cycling, indicating a correlation between redox activation and structural instability. Surface analysis *via* XPS indicates more stable surface chemistries, marked by higher transition metal oxidation states. W_2E_1 exhibits better cycling performance, having a specific capacity of more than 200 mAh g^{-1} at C/10 and a capacity retention of 84% at 1C after 250 cycles. These results highlight the impact of both bulk and surface structures on electrochemical functionality and demonstrate that synthesis parameters critically dictate defect formation and, consequently, the redox activity and cycling stability in Co-free LRLOs. Although establishing a direct correlation between structural features and electrochemical functionality remains challenging due to the intricate interdependence of bulk and surface structures, our findings offer mechanistic insights that advance the rational design of next-generation cobalt-free cathodes.

Author contributions

Arcangelo Celeste: conceptualization, methodology, investigation, visualization, writing – original draft. Valeria Lombardi: investigation. Marta Mirolo: investigation, writing – review & editing. Yan Lu: investigation, visualization, writing – review & editing. Rafal E. Dunin-Borkowski: writing – review & editing. Eric Hirschmann: investigation, writing – review & editing. Maik Butterling: investigation. Maciej Oskar Liedke: investigation. Andreas Wagner: investigation. Antonino Santoni: investigation. Priscilla Reale: investigation, visualization, writing – review & editing. Maria Assunta Navarra: writing – review & editing, supervision. Sergio Brutti: conceptualization, methodology, investigation, supervision, writing – original draft. Laura Silvestri: conceptualization, methodology, investigation, visualization, supervision, writing – original draft.

Conflicts of interest

There are no conflicts to declare.

Data availability

The data supporting this article have been included as part of the supplementary information (SI). Supplementary information is available. See DOI: https://doi.org/10.1039/d5ta06306j.

The diffraction datasets in Fig. 2 analyzed during the current study can be found in the ESRF Data Portal at https://doi.org/10.15151/ESRF-ES-1424924468.

Acknowledgements

L. S., P. R. and A. S. received funds from Ministero dell'Ambiente e della Sicurezza Energetica (MASE) in the framework of “Ricerca di Sistema Elettrico”. L. S. acknowledges the IPCEI project European Battery Innovation (EuBatIn) funded by Ministero dell'ambiente e della sicurezza energetica. The contribution of S. B., M. A. N., and A. C. to this study was carried out within the NEST—Network for Energy Sustainable Transition and received funding from the European Union Next-Generation EU (PIANO NAZIONALE DI RIPRESA E RESILIENZA (PNRR)—MISSIONE 4 COMPONENTE 2, INVESTIMENTO 1.3—D.D. 1561 11/10/2022, B53C22004070006). This manuscript reflects only the authors' views and opinions; neither the European Union nor the European Commission can be considered responsible for them. All Sapienza staff within the NEST project participated in this action under the framework of the grant PE2421852F05911E. The XRD synchrotron radiation experiments, TEM and PALS analysis were carried out in the framework of ReMade@ARI funded by the European union as part of the Horizon Europe call HORIZON-INFRA-2021-SERV-01 under grant agreement number 101058414 and co-funded by UK Research and Innovation (UKRI) under the UK government's Horizon Europe funding guarantee (grant number 10039728) and by the Swiss State Secretariat for Education, Research and Innovation (SERI) under contract number 22.00187. Views and opinions expressed are however those of the author(s) only and do not necessarily reflect those of the European Union or the UK Science and Technology Facilities Council or the Swiss State Secretariat for Education, Research and Innovation (SERI). Neither the European Union nor the granting authorities can be held responsible for them. We acknowledge the European Synchrotron Radiation Facility (ID22 beamline) for provision of synchrotron radiation facilities under proposal number XA-5.

References

1 P. G. Bruce, B. Scrosati and J. M. Tarascon, Nanomaterials for Rechargeable Lithium Batteries, *Angew. Chem., Int. Ed.*, 2008, **47**(16), 2930–2946, DOI: 10.1002/ANIE.200702505.

2 J. M. Tarascon, Na-Ion versus Li-Ion Batteries: Complementarity Rather than Competitiveness, *Joule*, 2020, **4**(8), 1616–1620, DOI: 10.1016/J.JOULE.2020.06.003.

3 C. P. Grey and D. S. Hall, Prospects for Lithium-Ion Batteries and beyond—a 2030 Vision, *Nat. Commun.*, 2020, **11**(1), 1–4, DOI: 10.1038/s41467-020-19991-4.

4 B. E. Murdock, K. E. Toghill, N. Tapia-Ruiz, B. E. Murdock, K. E. Toghill and N. Tapia-Ruiz, A Perspective on the Sustainability of Cathode Materials Used in Lithium-Ion Batteries, *Adv. Energy Mater.*, 2021, **11**(39), 2102028, DOI: 10.1002/AENM.202102028.

5 S. Dühnen, J. Betz, M. Kolek, R. Schmuch, M. Winter, T. S. Placke Dühnen, J. Betz, M. Kolek, R. Schmuch, M. Winter and T. Placke, Toward Green Battery Cells: Perspective on Materials and Technologies, *Small Methods*, 2020, **4**(7), 2000039, DOI: 10.1002/SMTD.202000039.

6 X. Yu and A. Manthiram, Sustainable Battery Materials for Next-Generation Electrical Energy Storage, *Adv. Energy Sustainability Res.*, 2021, **2**(5), 2000102, DOI: 10.1002/AESR.202000102.

7 L. Silvestri, A. Celeste, M. Tuccillo and S. Brutti, Li-Rich Layered Oxides: Structure and Doping Strategies to Enable Co-Poor/Co-Free Cathodes for Li-Ion Batteries, *Crystals*, 2023, **13**(2), 204, DOI: 10.3390/CRYST13020204.

8 J. Wang, X. He, E. Paillard, N. Laszczynski, J. Li and S. Passerini, Lithium- and Manganese-Rich Oxide Cathode Materials for High-Energy Lithium Ion Batteries, *Adv. Energy Mater.*, 2016, **6**(21), 1600906, DOI: 10.1002/AENM.201600906.

9 A. Celeste, M. Tuccillo, A. S. Menon, W. Brant, D. Brandell, V. Pellegrini, R. Brescia, L. Silvestri and S. Brutti, On the Elusive Crystallography of Lithium-Rich Layered Oxides: Novel Structural Models, *Small Methods*, 2024, **8**(9), 2301466, DOI: 10.1002/SMTD.202301466.

10 E. M. Erickson, F. Schipper, T. R. Penki, J.-Y. Shin, C. Erk, F.-F. Chesneau, B. Markovsky and D. Aurbach, Review—Recent Advances and Remaining Challenges for Lithium Ion Battery Cathodes, *J. Electrochem. Soc.*, 2017, **164**(1), A6341, DOI: 10.1149/2.0461701JES.

11 K. A. Jarvis, Z. Deng, L. F. Allard, A. Manthiram and P. J. Ferreira, Atomic Structure of a Lithium-Rich Layered Oxide Material for Lithium-Ion Batteries: Evidence of a Solid Solution, *Chem. Mater.*, 2011, **23**, 3614–3621, DOI: 10.1021/cm200831c.

12 C. C. Genevois, H. Koga, L. Croguennec, M. Ménétrier, M. Ménétrier, C. Delmas and F. Ois Weill, Insight into the Atomic Structure of Cycled Lithium-Rich Layered Oxide $Li_{1.20}Mn_{0.54}Co_{0.13}Ni_{0.13}O_2$ Using HAADF STEM and Electron Nanodiffraction, *J. Phys. Chem. C*, 2014, **119**(1), 75–83, DOI: 10.1021/jp509388j.

13 A. R. Armstrong, M. Holzapfel, P. Novk, S. Christopher, S. Kang, M. M. Thackeray, P. G. Bruce, L. Ni, L. Mn, P. Nova and C. S. Johnson, Demonstrating Oxygen Loss and Associated Structural Reorganization in the Lithium Battery Cathode Li [Ni Li Mn] O, *J. Am. Chem. Soc.*, 2006, **128**(11), 8694–8698, DOI: 10.1021/JA062027.

14 V. Pimenta, M. Sathiya, D. Batuk, A. M. Abakumov, D. Giaume, S. Cassaignon, D. Larcher and J. M. Tarascon, Synthesis of Li-Rich NMC: A Comprehensive Study, *Chem. Mater.*, 2017, **29**(23), 9923–9936, DOI: 10.1021/ACS.CHEMMATER.7B03230.

15 A. Celeste, F. Girardi, L. Gigli, V. Pellegrini, L. Silvestri and S. Brutti, Impact of Overlithiation and Al Doping on the Battery Performance of Li-Rich Layered Oxide Materials, *Electrochim. Acta*, 2022, **428**, 140737, DOI: 10.1016/j.electacta.2022.140737.

16 T. Zhao, J. Zhang, K. Wang, Y. Xiao, Q. Wang, L. Li, J. Tseng, M. Chen, J. Ma, Y. Lu, I. Hirofumi, Y. Shao, X. Zhao, S. Hung, Y. Su, X. Mu and W. Hua, Exploring the Mechanism of Surface Cationic Vacancy Induces High Activity of Metastable Lattice Oxygen in Li- and Mn-Rich Cathode Materials, *Angew. Chem., Int. Ed.*, 2025, **64**(21), e202508980, DOI: 10.1002/anie.202419664.

17 W. Hua, J. Chen, D. Ferreira Sanchez, B. Schwarz, Y. Yang, A. Senyshyn, Z. Wu, C. Shen, M. Knapp, H. Ehrenberg, S. Indris, X. Guo and X. Ouyang, Probing Particle-Carbon/Binder Degradation Behavior in Fatigued Layered Cathode Materials through Machine Learning Aided Diffraction Tomography, *Angew. Chem.*, 2024, **136**(30), e202403189, DOI: 10.1002/anie.202403189.

18 F. Fu, Y. Huang, P. Wu, Y. Bu, Y. Wang and J. Yao, Controlled Synthesis of Lithium-Rich Layered Li1.2Mn0.56Ni0.12Co0.12O2 Oxide with Tunable Morphology and Structure as Cathode Material for Lithium-Ion Batteries by Solvo/Hydrothermal Methods, *J. Alloys Compd.*, 2015, **618**, 673–678, DOI: 10.1016/J.JALLCOM.2014.08.191.

19 F. Fu, Y. P. Deng, C. H. Shen, G. L. Xu, X. X. Peng, Q. Wang, Y. F. Xu, J. C. Fang, L. Huang and S. G. Sun, A Hierarchical Micro/Nanostructured 0.5Li2MnO3·0.5LiMn0.4Ni0.3Co0.3O2 Material Synthesized

by Solvothermal Route as High Rate Cathode of Lithium Ion Battery, *Electrochem. Commun.*, 2014, **44**, 54–58, DOI: 10.1016/J.ELECOM.2014.04.013.

20 G. Wang, L. Yi, R. Yu, X. Wang, Y. Wang, Z. Liu, B. Wu, M. Liu, X. Zhang, X. Yang, X. Xiong and M. Liu, Li1.2Ni0.13Co0.13Mn0.54O2 with Controllable Morphology and Size for High Performance Lithium-Ion Batteries, *ACS Appl. Mater. Interfaces*, 2017, **9**(30), 25358–25368, DOI: 10.1021/ACSAMI.7B07095.

21 M. Malik, K. H. Chan and G. Azimi, Review on the Synthesis of LiNixMnyCo1-x-YO2 (NMC) Cathodes for Lithium-Ion Batteries, *Mater. Today Energy*, 2022, **28**, 101066, DOI: 10.1016/J.MTENER.2022.101066.

22 Y. Shao, C. Li, L. Li, J. Liu and S. Liao, Morphology-Tuned Porous Lithium-Rich Cathode Materials Synthesized via a Solvothermal Approach for Li-Ion Battery Application, *ACS Appl. Energy Mater.*, 2023, **6**(4), 2531–2540, DOI: 10.1021/ACSAEM.2C03971.

23 W. Yan, J. Jiang, W. Liu, D. Sun, E. Zhao, Y. Jin and K. Kanamura, Effect of Precipitators on the Morphologies and Electrochemical Properties of Li1.2Mn0.54Ni0.13Co0.13O2 via Rapid Nucleation and Post-Solvothermal Method, *Electrochim. Acta*, 2017, **224**, 161–170, DOI: 10.1016/J.ELECTACTA.2016.12.035.

24 A. Celeste, M. Paolacci, P. G. Schiavi, S. Brutti, M. A. Navarra and L. Silvestri, Understanding the Impact of Fe-Doping on the Structure and Battery Performance of a Co-Free Li-Rich Layered Cathodes, *ChemElectroChem*, 2023, **10**(5), e202201072, DOI: 10.1002/CELC.202201072.

25 C. Dejoie, M. Coduri, S. Petitdemange, C. Giacobbe, E. Covacci, O. Grimaldi, P. O. Autran, M. W. Mogodi, D. Š. Jung and A. N. Fitch, Combining a Nine-Crystal Multi-Analyser Stage with a Two-Dimensional Detector for High-Resolution Powder X-Ray Diffraction, *Appl. Crystallogr.*, 2018, **51**(6), 1721–1733, DOI: 10.1107/S1600576718014589.

26 A. Fitch, C. Dejoie, E. Covacci, G. Confalonieri, O. Grendal, L. Claustre, P. Guillou, J. Kieffer, W. De Nolf, S. Petitdemange, M. Ruat and Y. Watier, ID22 - the High-Resolution Powder-Diffraction Beamline at ESRF, *J. Synchrotron Radiat.*, 2023, **30**(5), 1003–1012, DOI: 10.1107/S1600577523004915.

27 M. Casas-Cabanas, M. Reynaud, J. Rikarte, P. Horbach and J. Rodríguez-Carvajal, FAULTS: A Program for Refinement of Structures with Extended Defects, *J. Appl. Crystallogr.*, 2016, **49**(6), 2259–2269, DOI: 10.1107/S1600576716014473.

28 A. Wagner, M. Butterling, M. O. Liedke, K. Potzger and R. Krause-Rehberg, Positron Annihilation Lifetime and Doppler Broadening Spectroscopy at the ELBE Facility, *AIP Conf. Proc.*, 2018, **1970**(1), 40003, DOI: 10.1063/1.5040215/660121.

29 E. Hirschmann, M. Butterling, U. Hernandez Acosta, M. O. Liedke, A. G. Attallah, P. Petring, M. Görler, R. Krause-Rehberg and A. Wagner, A New System for Real-Time Data Acquisition and Pulse Parameterization for Digital Positron Annihilation Lifetime Spectrometers with High Repetition Rates, *J. Instrum.*, 2021, **16**(08), P08001, DOI: 10.1088/1748-0221/16/08/P08001.

30 R. Krause-Rehberg and H. S. Leipner, *Positron Annihilation in Semiconductors: Defect Studies*, 1999, vol. 127, DOI: 10.1007/978-3-662-03893-2.

31 J. V. Olsen, P. Kirkegaard, N. J. Pedersen and M. Eldrup, PALSfit: A New Program for the Evaluation of Positron Lifetime Spectra, *Phys. Status Solidi C*, 2007, **4**(10), 4004–4006, DOI: 10.1002/PSSC.200675868.

32 J. Dryzek and P. Horodek, GEANT4 Simulation of Slow Positron Beam Implantation Profiles, *Nucl. Instrum. Methods Phys. Res., Sect. B*, 2008, **266**(18), 4000–4009, DOI: 10.1016/J.NIMB.2008.06.033.

33 A. Celeste, M. Tuccillo, A. Santoni, P. Reale, S. Brutti and L. Silvestri, Exploring a Co-Free, Li-Rich Layered Oxide with Low Content of Nickel as a Positive Electrode for Li-Ion Battery, *ACS Appl. Energy Mater.*, 2021, **4**(10), 11290–11297, DOI: 10.1021/ACSAEM.1C02133.

34 S. Ma, Inter-Molecular Interactions between Water and Ethanol, *Adv. Sci. Technol. Res. J.*, 2023, **4**(1), 515, DOI: 10.56028/AETR.4.1.515.2023.

35 F. Llovell, O. Vilaseca, N. Jung and L. F. Vega, Water + 1-Alkanol Systems: Modeling the Phase, Interface and Viscosity Properties, *Fluid Phase Equilib.*, 2013, **360**, 367–378, DOI: 10.1016/J.FLUID.2013.10.002.

36 Q. Dong, C. Yu, L. Li, L. Nie, D. Li and H. Zang, Near-Infrared Spectroscopic Study of Molecular Interaction in Ethanol-Water Mixtures, *Spectrochim. Acta, Part A*, 2019, **222**, 117183, DOI: 10.1016/J.SAA.2019.117183.

37 G. Ma, S. Li, E. Zhang, Z. Yang, S. Liu, X. Fan, F. Hen, Y. Tian, W. Zhang, S. Hihe Yang, M. Li, G. Ma, S. Li, W. X. Zhang, Z. H. Y. Ang, S. L. Liu, X. M. F. An, F. Chen, Y. Tian, W. B. Zhang, S. H. Y. Ang and M. Li, A General and Mild Approach to Controllable Preparation of Manganese-Based Micro- and Nanostructured Bars for High Performance Lithium-Ion Batteries, *Angew. Chem., Int. Ed.*, 2016, **55**(11), 3667–3671, DOI: 10.1002/ANIE.201511196.

38 D. B. Bautista, M. Aguilar and O. Pizio, Molecular Dynamics Simulations of Water-Ethanol Mixtures. I. Composition Trends in Thermodynamic Properties, *Condens. Matter Phys.*, 2024, **27**(2), 23201, DOI: 10.5488/cmp.27.23201.

39 A. Ghoufi, F. Artzner and P. Malfreyt, Physical Properties and Hydrogen-Bonding Network of Water-Ethanol Mixtures from Molecular Dynamics Simulations, *J. Phys. Chem. B*, 2016, **120**(4), 793–802, DOI: 10.1021/ACS.JPCB.5B11776.

40 J. Cardona, M. B. Sweatman and L. Lue, Molecular Dynamics Investigation of the Influence of the Hydrogen Bond Networks in Ethanol/Water Mixtures on Dielectric Spectra, *J. Phys. Chem. B*, 2018, **122**(4), 1505–1515, DOI: 10.1021/ACS.JPCB.7B12220.

41 P. Petong, R. Pottel and U. Kaatze, Water-Ethanol Mixtures at Different Compositions and Temperatures. A Dieletric Relaxation Study, *J. Phys. Chem. A*, 2000, **104**(32), 7420–7428, DOI: 10.1021/JP001393R.

42 A. V. Navarkhele and V. V. Navarkhele, Static Dielectric Constants, Densities, Refractive Indices and Related Properties of Binary Mixtures at Various Temperatures

Under Atmospheric Pressure, *Int. J. Thermodyn.*, 2022, **25**(3), 1–10, DOI: 10.5541/IJOT.1017174.

43 D. Pečar and V. Doleček, Volumetric Properties of Ethanol–Water Mixtures under High Temperatures and Pressures, *Fluid Phase Equilib.*, 2005, **230**(1–2), 36–44, DOI: 10.1016/J.FLUID.2004.11.019.

44 J. Yuan, X. L. Shi, D. Z. Wang, W. Di Liu, M. Li, W. Chen, Q. Yang, Y. Wang, Q. Liu and Z. G. Chen, Tuning the Saturated Vapor Pressure of Solvothermal Synthesis to Boost the Thermoelectric Performance of Pristine Bi2Te3 Polycrystals by Anisotropy Strengthening, *ACS Appl. Energy Mater.*, 2023, **6**(11), 6227–6236, DOI: 10.1021/ACSAEM.3C00755.

45 P. S. Badajoz, D. García-Vera, P. Herrera-Vega and A. Marrero-Pérez, High-Pressure Phase Equilibria in an Ethanol/Water Binary System: Experimental Data and Modeling, *J. Chem. Eng. Data*, 2021, **66**(2), 928–946, DOI: 10.1021/ACS.JCED.0C00686.

46 D. Kramer and G. Ceder, Tailoring the morphology of LiCoO2: a first principles study, *Chem. Mater.*, 2009, **21**(16), 3799–3809, DOI: 10.1021/cm9008943.

47 R. T. Haasch and D. P. Abraham, Lithium-Based Transition-Metal Oxides for Battery Electrodes Analyzed by x-Ray Photoelectron Spectroscopy. VIII. Li1.2Ni0.15Co0.1Mn0.55O2, *Surf. Sci. Spectra*, 2019, **26**(1), DOI: 10.1116/1.5080240.

48 E. S. Ilton, J. E. Post, P. J. Heaney, F. T. Ling and S. N. Kerisit, XPS Determination of Mn Oxidation States in Mn (Hydr) Oxides, *Appl. Surf. Sci.*, 2016, **366**, 475–485, DOI: 10.1016/J.APSUSC.2015.12.159.